ARTICLES

Synthesis, Structure, and Photocatalysis in a New Structural Variant of the Aurivillius Phase: LiBi₄M₃O₁₄ (M = Nb, Ta)

B. Muktha,[†] M. H. Priya,[‡] Giridhar Madras,[‡] and T. N. Guru Row*,[†]

Solid State and Structural Chemistry Unit and Department of Chemical Engineering, Indian Institute of Science, Bangalore 560012, India

Two new compounds, $LiBi_4Nb_3O_{14}$ and $LiBi_4Ta_3O_{14}$, have been synthesized by the solid-state method, using Li_2CO_3, Bi_2O_3, and M_2O_5 (M = Nb, Ta) in stoichiometric quantities. These compounds crystallize in the monoclinic $C2/c$ space group with $a = 13.035(3)$ Å, $b = 7.647(2)$ Å, $c = 12.217(3)$ Å, $\beta = 101.512(4)°$, $V = 1193.4(5)$ Å³, and $Z = 4$ and $a = 13.016(2)$ Å, $b = 7.583(1)$ Å, $c = 12.226(2)$ Å, $\beta = 101.477(3)°$, $V = 1182.6(5)$ Å³, and $Z = 4$, respectively. These are isostructural and the structure along the b axis consists of layers of $[Bi_2O_2]^{2+}$ units separated by layers of LiO_4 tetrahedra and NbO_6 octahedra hence depicting an unusual variation in the Aurivillius phase isolated for the first time. The presence of lithium has been confirmed by ⁷Li NMR studies. ac impedance measurements and variable temperature ⁷Li NMR studies indicate oxygen ion conductivity in these materials. The UV–visible spectra suggest a band gap of 3.0 eV for $LiBi_4Nb_3O_{14}$ and 3.5 eV for $LiBi_4Ta_3O_{14}$, respectively, and the associated studies on degradation of dyes and phenols render these materials suitable for photocatalysis.

Introduction

The chemistry of layered oxides has become one of the most important areas of solid state chemistry largely driven by their structural and compositional flexibility which allows for control and design of novel chemical and physical properties such as catalysis,[1] ferroelectricity,[2] and ionic conductivity.[3] The Bi_2O_3–Nb_2O_5 and Bi_2O_3–Ta_2O_5 systems have been less investigated in terms of structure owing to complex modulations in the structure and their properties are not yet harnessed. The only phases known in these systems are $Bi_3Nb_{17}O_{47}$,[4] $BiNbO_4$,[5,6] Bi_3-NbO_7,[7] $Bi_7Ta_3O_{18}$,[8] $Bi_4Ta_2O_{11}$,[9] and $BiTaO_4$,[10] and it is to be noted that all these phases have a fluorite related structure. $BiNbO_4$ and $BiTaO_4$ show polymorphic modifications at different temperatures of synthesis, the low-temperature orthorhombic form (900 °C) and the high-temperature triclinic form (1100 °C). Both the forms are isostructural and the structures consist of chains of $(Nb/Ta)O_6$ octahedra separated by Bi atoms. Photocatalytic reactions of $BiTaO_4$ (with substitution of Nb in various concentrations at the Ta site) in an aqueous CH_3OH/H_2O solution with 0.1 wt % of catalyst loading show higher rates in case of the orthorhombic forms than the triclinic forms[10,11] in accordance with lower band gaps of the orthorhombic forms. Advances in materials fabrication led to the discovery of metal oxide semiconductors with tunnel or layered perovskite structures with specific applications such as decomposition of water under UV radiation.[12,13] Recently, niobates and tantalates consisting of corner shared NbO_6 or TaO_6 octahedra have been of interest due to their optoelectronic and efficient luminescence properties.[14] In search of new and novel photocatalysts, bismuth niobates and tantalates hold promise as they are expected to provide structural motifs suitable for generating band gaps in the UV region.

The application of semiconductor photocatalysts in wastewater treatment, water and air purification, cleanup of oil spills, photosplitting of water to produce hydrogen gas, and other problems of environmental interest has grown immensely.[15] Simple oxide and sulfide semiconductors have band gap energies sufficient for promoting or catalyzing these chemical reactions of environmental interest. However, among all the semiconductors, TiO_2 (Degussa P25) has proven to be the most suitable for widespread environmental applications such as remediation of hazardous wastes and contaminated groundwaters, control of toxic air contaminants, removal of toxic dyes from the industrial effluents, photosplitting of water, and cleanup of oil spills.[15]

The primary criteria for good semiconductor photocatalysts for the degradation of an organic compound are that the redox potential of the H_2O/⁻OH (OH⁻ + e⁻; $E^0 = -2.8$ eV) couple lies within the band gap domain of the material and that they are stable over prolonged periods of time.[15] When a photon of energy $h\nu$ matches or exceeds the band gap, E_g, of the semiconductor, an electron, e_{cb}^-, is promoted from the valence band VB to the conduction band CB, leaving a hole, $h\nu_b^+$ behind. Excited-state conduction band electrons can then recombine with the valence band holes, dissipate the input energy, and get trapped in meta stable surface states. On the other hand, they can react with the electron donors and acceptors adsorbed on the semiconductor surface or within the surrounding electrical double layer of the charged particles.

The application of illuminated semiconductors for remediation of contaminants has been used in a variety of compounds such

* Address correspondence to this author. Phone: +91-80-22932796, +91-80-22932336. Fax: +91-80-23601310. E-mail: ssctng@sscu.iisc.ernet.in.
† Solid State and Structural Chemistry Unit.
‡ Department of Chemical Engineering.

New Structural Variant of the Aurivillius Phase

J. Phys. Chem. B, Vol. 109, No. 23, 2005 **11443**

as alkanes, aliphatic alcohols, aliphatic carboxylic acids, alkenes, phenols, aromatic carboxylic acids, dyes, and pesticides, as well as for reductive deposition of heavy metals (e.g., Pt^{4+}, Au^{3+}, Rh^{3+}) from aqueous solutions to surfaces.[16-27] In many cases complete mineralization of organic compounds has been reported.

Pyrochlore materials of the type Bi_2ANbO_7 (A = Al^{3+}, Ga^{3+}, In^{3+}) show higher activity than that of TiO_2 in the decomposition of $Pt/CH_3OH/H_2O$ solution.[28] The structure consists of chains of a three-dimensional network of MO_6 stacked along [001] while chains of NbO_6 octahedra and the Bi atoms are located in the three-dimensional network of MO_6. The band gap is lowered on substitution of Al^{3+} to Ga^{3+} to In^{3+} from 2.9 to 2.7 eV due to a decrease in the ionic radii leading to a difference in the photocatalytic behavior. Bismuth niobates of the type $ABi_2Nb_2O_9$ show structures similar to that of the Aurivillius phases, while those of the form $A_2Bi_2Nb_2O_6$, where A = alkaline earth metal or Pb, have a layered perovskite structure and $ABi_2Nb_2O_9$, where A = Ni, Mg, Zn, have a cubic pyrochlore structure. So far in the literature, there is only one report of a lithium doped bismuth niobate, $Li_{0.29}Bi_{2.53}Nb_2O_9$,[29] isostructural with that of the Aurivillius[30] phase of the general formula $Bi_2A_{m-1}B_mO_{3m+3}$ (m = 1, 2, 3, 4). The aim of generating new structural types in the $Li_2O-Bi_2O_3-(Ta/Nb)_2O_5$ systems is essentially to devise materials with band gaps sufficient to aid enhanced photocatalytic activity. In this context, we have synthesized and characterized $LiBi_4Ta_3O_{14}$ and $LiBi_4Nb_3O_{14}$ for the first time. It is of interest to note that the titanium analogue of the title compounds, $Li_2Bi_4Ti_3O_{12}$, is an Aurivillius oxide.[31] Further, $LiBi_4Ta_3O_{14}$ and $LiBi_4Nb_3O_{14}$ were used in the photodegradation of a wide range of commonly used (azo and non azo) dyes in the textile industry like Alizarin Red S (AS), Alizarine cyanine Green (AG), Coomassie Brilliant Blue (CB), Orange G (OG), and Methyl Violet (MV) and phenolic compounds.

Experimental Section

Materials. Bi_2O_3 (Fluka, 99.99%) and Nb_2O_5 (Sigma Aldrich, 99.99%) were dried at 600 °C while Ta_2O_5 (Sigma Aldrich, 99.99%) was dried at 700 °C before syntheses. Li_2CO_3 (Fluka, 99%) was used as such. Alizarin Red S, Methyl Violet MS, Orange G, phenol, and 4-nitrophenol (all from S. D. fine-Chem Ltd, India), Alizarine cyanine Green (Rolex, India), and Coomassie Brilliant Blue R250 (Merck, India) were used as received. Water was double distilled and filtered through a Millipore membrane filter prior to use.

Preparation. $LiBi_4Nb_3O_{14}$ and $LiBi_4Ta_3O_{14}$ were synthesized by the solid-state method with use of Li_2CO_3, Bi_2O_3, Nb_2O_5, and Ta_2O_5 in stoichiometric quantities. The starting materials were ground well in an agate mortar and fired at 950 °C for 2 h. Preliminary powder X-ray patterns confirm the formation of a single phase. Several phases appear upon prolonged heating at temperatures greater than 700 °C. To ascertain if these phases were lithium rich, $LiBi_4Nb_3O_{14}$ was synthesized with double the lithium content. This yielded five different phases on melting. A careful examination under the polarizing microscope revealed the presence of yellow $LiBi_4Nb_3O_{14}$ (major phase) and colorless, orange, red, and deep brown (minor phases) crystals. Yellow single crystals of $LiBi_4Nb_3O_{14}$ were obtained by the melt cooling technique from the original stoichiometries. The reaction mixture was melted at 1170 °C in a platinum crucible and slowly cooled at the rate of 1 °C/min up to 1150 °C and then furnace cooled to room temperature. Single crystals of $LiBi_4Ta_3O_{14}$ were obtained by melting the powder at 1250 °C

and slowly cooled at 1 °C /min to 1235 °C and then furnace cooled to room temperature to yield pale yellow single crystals of $LiBi_4Ta_3O_{14}$.

Characterization. The Bi/Nb and Bi/Ta ratio on several yellow single crystals of $LiBi_4Nb_3O_{14}$ and $LiBi_4Ta_3O_{14}$, respectively, were determined by energy-dispersive X-ray (EDX) microanalysis on a JEOL JSM-840 SEM/EDAX machine. BET analysis by gas sorption was conducted with Quantachrome Nova 2200 to determine the surface area of the materials.

Single-Crystal X-ray Diffraction. Single-crystal X-ray diffraction data were collected on a Bruker Axs SMART APEX CCD diffractometer[32] with a crystal-to-detector distance of 6.06 cm. The data were collected based on 3 sets of runs covering a complete sphere of reciprocal space with each set at a different φ angle (φ = 0, 90°, 180°). Each frame covered 0.3° in ω. The data were reduced with SAINT PLUS[32] and the structure was solved by direct and Patterson methods with SHELXS97 and refined with SHELXL97.[33] Crystallographic data and the details of the single-crystal data collection are given in Table 1. The bond valence sums have been calculated according to the method of Brown and Shannon[34,35] (Table 2a,b).

The colorless crystals in the case of lithium rich $LiBi_4Nb_3O_{14}$ corresponded to Li_3NbO_4.[36] The orange crystals could be indexed into the orthorhombic system with a = 11.921(3) Å, b = 8.427(2) Å, c = 11.926(3) Å, V = 1198.12(6) Å^3. Space group Fmm2 (no. 42) was assigned based on the systematic absences, and values of h, k, l: all odd or all even reflections for F centering. The other minor phases did not yield good quality single crystals.

^{7}Li NMR spectra of the compounds were obtained on a DSX 300 Bruker spectrometer equipped with a 5-mm MAS probe head. A solution of 1 M LiCl was used as reference. The UV–visible diffuse reflectance spectra were recorded on a Lambda 32 Perkin-Elmer UV–visible spectrophotometer. DTA plots of the samples were obtained under a constant flow nitrogen atmosphere on a SDTQ600 DSC/DTA instrument.

ac Impedance. Circular pellets of both compounds of about 10-mm thickness were sintered at 500 °C. The compounds were then sputtered with gold for ac impedance measurements. Each sample was then mounted in an impedance jig and placed in a tube furnace where the temperature was controlled to ±3 °C over the range 30–600 °C. ac impedance measurements were carried out between 5 Hz and 13 MHz on a Hewlett-Packard HP4192A impedance gain phase analyzer. A home-built cell assembly with a 2-terminal capacitor configuration and stainless steel electrodes were used for the experiment. The sample temperature was measured with a Pt–Rh thermocouple positioned very close to the sample. The frequency dependence of the impedance was measured between 30 and 600 °C in a heating–cooling cycle. The samples were equilibrated for half an hour at every temperature. The ionic conductivity was calculated from the intercept of the single semicircular arcs obtained in the complex impedance plots.

Photocatalytic Experiments: Photochemical Reactor. The photochemical reactor employed in this study was comprised of a jacketed quartz tube of 3.4 cm id, 4 cm od, and 21 cm length and an outer Pyrex glass reactor of 5.7 cm id and 16 cm length. A high-pressure mercury vapor lamp (HPML) of 125 W (Philips, India) was placed inside the jacketed quartz tube after removal of the outer shell. The ballast and capacitor were connected in series with the lamp to avoid the fluctuations in the input supply. Water was circulated through the annulus of the quartz tube to avoid heating of the solution due to dissipative loss of UV energy. The solution was taken in the outer reactor

TABLE 1: Crystallographic Data for LiBi$_4$Ta$_3$O$_{14}$ and LiBi$_4$Nb$_3$O$_{14}$

	LiBi$_4$Nb$_3$O$_{14}$	LiBi$_4$Ta$_3$O$_{14}$
empirical formula	LiBi$_4$Nb$_3$O$_{14}$	LiBi$_4$Ta$_3$O$_{14}$
crystal habit, color	cylindrical, yellow	cylindrical, yellow
crystal size (cm^3)	0.086 × 0.131 × 0.248	0.084 × 0.073 × 0.062
crystal system	monoclinic	monoclinic
space group	C2/c	C2/c
cell dimensions		
a (Å)	13.035(3)	13.016(2)
b (Å)	7.647(2)	7.5832(14)
c (Å)	12.217(3)	12.226(2)
β (deg)	101.512(4)	101.477(3)
volume (Å^3)	1193.4(5)	1182.6(4)
formula wt	1345.54	1602.77
density (calcd) (g/cm^3)	7.451	9.002
Z	4	4
F(000)	2268	2652
scan mode	ω scan	ω scan
θ range (deg)	3.1−26.37	3.13−28.03
recording reciprocal space	−16 ≤ h ≤ 15, 0 ≤ k ≤ 9, 0 ≤ l ≤ 15	−11 ≤ h ≤ 17, 9 ≤ k ≤ 6, −15 ≤ l ≤ 15
no. of measured reflns	1227	1365
no. of independent reflns	1194 [R(int) = 0.0443]	1184 [R(int) = 0.0443]
μ (mm^{-1})	61.621	87.013
no. of refined parameters	96	96
R[$I > 4\sigma I$]/R [all data]	0.0571/0.0576	0.0781/0.0827
WR[$I > 4\sigma$I]/R [all data]	0.1626/0.1631	0.1927/0.2005
GoF	1.27	1.076
max/min $\Delta\rho$ (e/Å)^3	4.457/−7.548	8.522/−12.827

and continuously stirred to ensure that the suspension of the catalyst was uniform. The lamp radiated predominantly at 365 nm corresponding to the energy of 3.4 eV and photon flux is 5.8×10^{-6} mol of photons/s. Further details of the experimental setup can be found elsewhere.[37]

Degradation Experiments. The dyes/phenolic compounds are dissolved in double distilled Millipore filtered water and degraded in the photochemical reactor described above. The effect of the initial concentration of these organics and the effect of catalyst loading on the reaction rates were investigated. The reactions were carried out at 40 °C, which was maintained by circulating water in the annulus of the jacketed quartz reactor. Samples were collected at regular intervals, filtered through Millipore membrane filters, and centrifuged to remove the catalyst particles prior to analysis, as described below.

Sample Analysis. Samples were analyzed with a Lambda 32 Perkin-Elmer UV−visible spetrophotometer. The calibration for AS, AG, CB, OG, MV, phenol, and 4-nitrophenol was based on the Beer−Lambert law at its maximum absorption wavelength, λ_{max}, of 426, 626, 556, 547, 582, 270, and 320 nm, respectively.

Results and Discussion

Crystal Structure. The compositions of the samples were determined from an 8 EDX point analysis on the yellow single-crystal surfaces. The Bi/Nb and Bi/Ta ratio thus calculated from the EDAX analyses corresponded to that of the compositions taken initially for syntheses of LiBi$_4$Nb$_3$O$_{14}$ and LiBi$_4$Ta$_3$O$_{14}$, respectively.

The yellow compound LiBi$_4$Nb$_3$O$_{14}$ crystallized into the monoclinic C2/c system (no. 15) with $a = 13.035(3)$ Å, $b = 7.647(2)$ Å, $c = 12.217(3)$ Å, $\beta = 101.512(4)°$, $V = 1193.4(5)$ Å^3, and $Z = 4$. The positions of the Bi and Nb atoms were obtained by direct methods and all the remaining oxygen atoms in the structure were located by difference Fourier synthesis. Further, the residual electron density map showed a peak of 4 e/Å^3 at the 4e site, which was assigned to the Li atom. The coordinates of the lithium could not be refined due to the unreliable accuracy in the presence of heavy Bi atoms. The final cycles of refinement led to a final $R = 0.057$. The bond valence

TABLE 2: Bond Valence Sum for LiBi$_4$Nb$_3$O$_{14}$ and LiBi$_4$Ta$_3$O$_{14}$

(a) LiBi$_4$Ta$_3$O$_{14}$			
Bi(1)−O(3)	2.682(14)	Bi(2)−O(1)	2.653(15)
Bi(1)−O(4)	2.675(16)	Bi(2)−O(2)	2.744(14)
Bi(1)−O(4′)	2.228(17)	Bi(2)−O(4)	2.390(15)
Bi(1)−O(5)	2.183(15)	Bi(2)−O(5)	2.513(15)
Bi(1)−O(5′)	2.692(16)	Bi(2)−O(6)	2.801(14)
Bi(1)−O(6)	2.176(14)	Bi(2)−O(7)	2.143(17)
Bi(1)−O(7)	2.535(16)	Bi(2)−O(7′)	2.183(17)
valence sum	3.434	valence sum	3.055
Nb(1)−O(1)	1.844(15)	Nb(2)−O(2) × 2	2.076(16)
Nb(1)−O(1′)	2.200(15)	Nb(2)−O(3) × 2	1.891(15)
Nb(1)−O(2)	1.948(16)	Nb(2)−O(5) × 2	2.022(15)
Nb(1)−O(3)	2.064(14)		
Nb(1)−O(4)	2.057(16)		
Nb(1)−O(6)	1.896(14)		
valence sum	5.122	valence sum	5.054

(b) LiBi$_4$Ta$_3$O$_{14}$			
Bi(1)−O(3)	2.212(15)	Bi(2)−O(1)	2.635(16)
Bi(1)−O(3′)	2.65(15)	Bi(2)−O(3)	2.531(15)
Bi(1)−O(4)	2.244(16)	Bi(2)−O(4)	2.377(17)
Bi(1)−O(4′)	2.665(17)	Bi(2)−O(6)	2.135(16)
Bi(1)−O(5)	2.174(14)	Bi(2)−O(6′)	2.184(15)
Bi(1)−O(6)	2.52(14)		
Bi(1)−O(7)	2.694(14)		
valence sum	3.383	valence sum	2.882
Ta(1) −O(1)	1.947(14)	Ta(2) −O(2) × 2	2.001(15)
−O(1′)	2.07(15)	−O(3) × 2	1.998(15)
−O(2)	1.99(14)	−O(7) × 2	1.93(15)
−O(4)	2.038(18)		
−O(5)	1.901(14)		
−O(7)	1.991(14)		
valence sum	5.191	valence sum	5.386

sums for the Bi and Nb atoms confirm the assignment of the atoms (Table 2a).

The pale yellow crystal of LiBi$_4$Ta$_3$O$_{14}$ crystallized into the monoclinic C2/c system, $a = 13.115(2)$ Å, $b = 7.583(1)$ Å, $c = 12.226(2)$ Å, $\beta = 101.477(3)°$, $V = 1182.6(5)$ Å^3, and $Z = 4$. An empirical absorption correction was applied. The positions of Bi and Ta atoms were located by the Patterson method and the oxygen atoms were obtained by difference Fourier synthesis. The position of the lithium atom could not be obtained due the
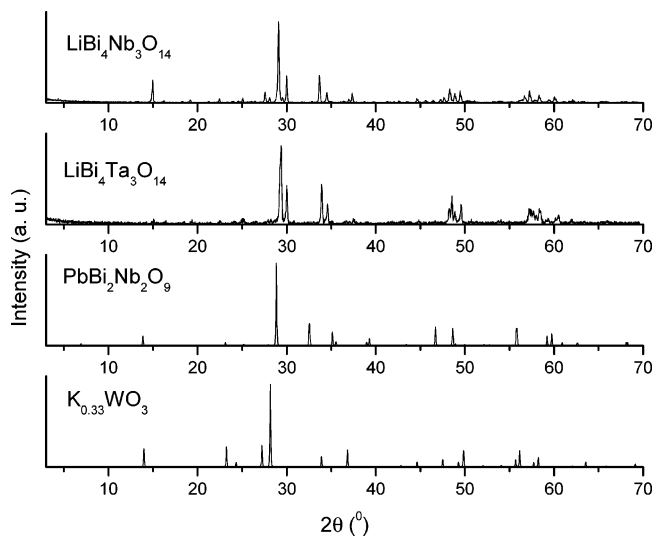
Figure 1. Powder X-ray patterns of $LiBi_4Nb_3O_{14}$, $LiBi_4Ta_3O_{14}$, $PbBi_2Nb_2O_9$, and $K_{0.33}WO_3$.

presence of heavy Bi and Ta atoms due to which the residual electron density could be located only around the Bi atoms. The final R index was 0.078. The assignment of the Bi and Ta atoms was further confirmed by the bond valence sums (Table 2b).

The powder X-ray patterns of the $LiBi_4(Nb/Ta)_3O_{14}$, Aurivillius phase[30] (for example, $PbBi_2Nb_2O_9$) and hexagonal tungsten bronzes[38] (HTB, for example, $K_{0.33}WO_3$) are shown in Figure 1. The 100I peak at $2\theta \approx 29°$ indicate the structural similarities with the Aurivillius phase. The 100I peak of $K_{0.33}$-WO_3 is shifted slightly. Since the powder patterns of $LiBi_4$-$(Nb/Ta)_3O_{14}$ do not match exactly with the reported Aurivillius phases and hexagonal tungsten bronzes, changes in the arrangement of the atoms and bonding features may be expected.

A view of the crystal structures along the b axis is shown in Figure 2a. The coordinates of the Li atoms obtained from the residual electron density were used to generate Figure 2a,b to visualize the arrangement of Li atoms in the crystal structure. The formula $LiBi_4(Nb/Ta)_3O_{14}$ may be represented as $[Bi_2O_2]$-$[LiO_4][(Nb/Ta)O_6]$. The structure consists of layers of $[Bi_2O_2]^{2+}$ units separated by layers of LiO_4 tetrahedra and $(Nb/Ta)O_6$ octahedra. Unlike in the Aurivillius phases, the A (Li in this case) atoms are not sandwiched between $(Nb/Ta)O_6$ octahedra, instead they occupy the T_+ (above the $(Nb/Ta)O_6$ layer) and T_- (below the $(Nb/Ta)O_6$ layer) sites alternately and occur along every alternate $(Nb/Ta)O_6$ layer. Lithium atoms share two corners with $[Bi_2O_2]^{2+}$ units and an edge with $(Nb/Ta)O_6$ octahedral units resulting in a new structural type in the Li_2O-Bi_2O_3-$(Nb/Ta)_2O_5$ system [Figure 2a,b]. The NbO_6 octahedra are interlinked to each other along both a and b axes [Figure 2b]. In $LiBi_4Nb_3O_{14}$, the Bi(1) and Bi(2) atoms are both coordinated to seven oxygen atoms forming BiO_7 polyhedra, while in $LiBi_4Ta_3O_{14}$, Bi(1) atoms form BiO_7 polyhedra and Bi(2) atoms form BiO_5 polyhedra. The effect of the $6s^2$ lone pair on Bi is evidenced by the distorted geometry of these polyhedra.

In $LiBi_4Nb_3O_{14}$, the Bi(1) atom has four relatively short bonds (2.176−2.535 Å) with O(4′), O(5), O(6), and O(7) and three long bonds (2.675−2.692 Å) with O(3), O(4), and O(5′). A similar coordination is depicted by Bi(2) with four relatively short bonds (2.143−2.513 Å) with O(4), O(5), O(7), and O(7′) and three long bonds (2.653−2.801 Å) with O(1), O(2), and O(6). Both Bi(1) and Bi(2) occupy general positions. The Nb-(1) and Nb(2) occupy the interstitial of NbO_6 octahedra. Nb(2)
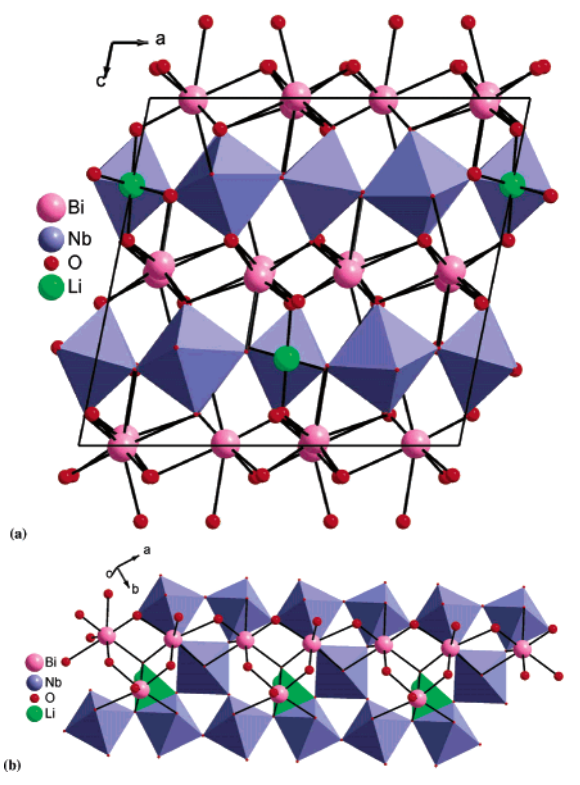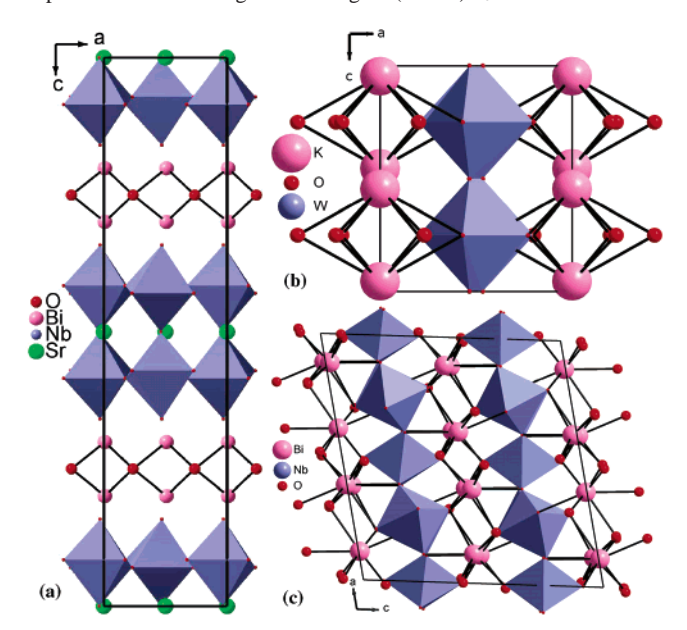

Figure 2. (a) A view of $LiBi_4(Nb/Ta)_3O_{14}$ along the b axis. (b) An expanded view showing interlinking of $(Nb/Ta)O_6$ octahedra.

Figure 3. Crystal structures of (a) $PbBi_2Nb_2O_9$, (b) K_xWO_3, and (c) $LiBi_4(Nb/Ta)_3O_{14}$.

occupies the 4e site. The bond lengths of Nb(1) and Nb(2) range between 1.844 and 2.200 and between 1.891 and 2.022 Å, respectively. The only other lithium bismuth niobate reported, $Li_{0.29}Bi_{2.53}Nb_2O_9$, has lithium atoms in trigonal prismatic coordination and the A site occupied by Li atoms and Bi atoms alternately is sandwiched between the NbO_6 octahedra.

$LiBi_4Ta_3O_{14}$ on the other hand has a Bi(1) atom with four relatively short bonds (2.174−2.520 Å) with O(3), O(4), O(5), and O(6) and three long bonds (2.65−2.694 Å) with O(3′), O(4′), and O(7). Bi(2) has four relatively short bonds (2.135−2.531 Å) with O(1), O(3), O(4), O(6), and O(6′) and one long bond with O(1) (2.635 Å). Both Bi(1) and Bi(2) occupy general positions. The Ta(1) and Ta(2) occupy the interstitial of the
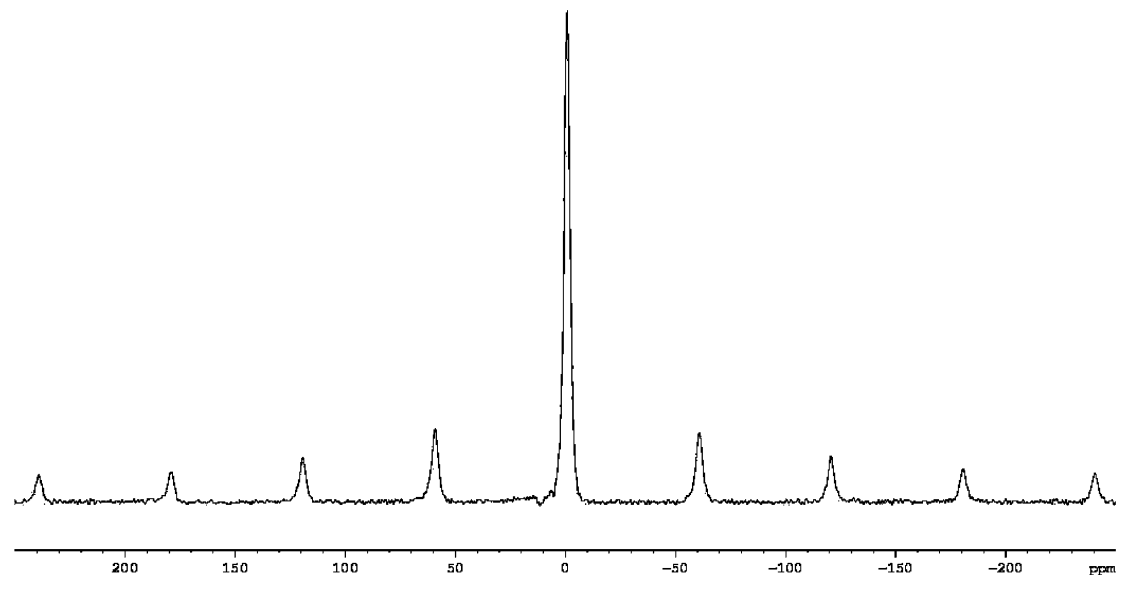
Figure 4. ^{7}Li MAS NMR spectrum of LiBi$_4$Nb$_3$O$_{14}$ at 7 kHz.

TaO$_6$ octahedra. Ta(2) occupies the 4e site. The bond lengths of Ta(1) and Ta(2) range between 1.901 and 1.991 and between 1.930 and 1.988 Å, respectively. Parts a–c of Figure 3 illustrate the differences between the Aurivillius phase, HTBs, and LiBi$_4$Nb$_3$O$_{14}$. It is of interest to note that the structure of LiBi$_4$(Nb/Ta)$_3$O$_{14}$ may also be related to HTBs of the type K$_x$WO$_3$ (x = 0.33) wherein the framework of the NbO$_6$ octahedra of LiBi$_4$Nb$_3$O$_{14}$ is similar to the layer of WO$_6$ octahedra in the HTB along the *b* axis.[32] However, the presence of [Bi$_2$O$_2$]$^{2+}$ layers and the absence of perovskite slabs makes LiBi$_4$(Nb/Ta)$_3$O$_{14}$ a closer relative of the Aurivillius phase than the HTBs . It is noteworthy that average Bi–O distances in the conventional Aurivillius phases generally range between 2.1 and 3.6 Å.[29–31] The bond angles O–(Nb/Ta)–O constituting the (Nb/Ta)O$_6$ octahedra in LiBi$_4$Nb$_3$O$_{14}$ and LiBi$_4$Ta$_3$O$_{14}$ differ considerably from that of the Aurivillius phases. All the oxygen atoms in the square plane of the (Nb/Ta)O$_6$ octahedra participate in the interlinking of the octahedra along the b and the c planes while the oxygen atoms at the apexes of the octahedra do not participate in the interlinking and instead are connected to the Bi atoms of the [Bi$_2$O$_2$] unit. The bond angles O(5)–Nb(2)-O(5) = 173.7(9)°, O(6)–Nb(1)–O(4) = 168.2(6)°, O(3)–Ta-(2)–O(3) = 178.7(8)°, and O(5)–Ta(1)–O(4) = 174.0(6)° corresponding to the apical oxygen atoms of the octahedra are larger than those of the Aurivillius phases which is ∼169°.

^{7}Li NMR Study. The ^{7}Li NMR spectrum of LiBi$_4$Nb$_3$O$_{14}$ suggests a singlet at −1.02 ppm confirming the presence of lithium. The spectrum exhibits a central line and spinning sidebands due to the first-order quadrupolar interaction [Figure 4]. LiBi$_4$Ta$_3$O$_{14}$ could not be spun hence a static spectrum of the sample was obtained (see the Supporting Information, Figure S1). To ascertain the mobility of Li in the compounds, variable-temperature ^{7}Li NMR studies were performed on LiBi$_4$Nb$_3$O$_{14}$. The samples were equilibrated for half an hour at each temperature. Measurements were done from room temperature up to 373 K in steps of 15 K. Figure 5 shows the plot of line width for a static sample at various temperatures. There is no significant change in the line width up to 373 K. Hence the mobility of Li within the lattice is negligible.

ac Impedance. ac impedance studies suggest conductivity values of 2.8 × 10^{-6} S cm^{-1} for LiBi$_4$Nb$_3$O$_{14}$ and 5.1 × 10^{-6} S cm^{-1} for LiBi$_4$Ta$_3$O$_{14}$ at 600 °C. Since the compounds decompose on prolonged heating at temperatures greater than
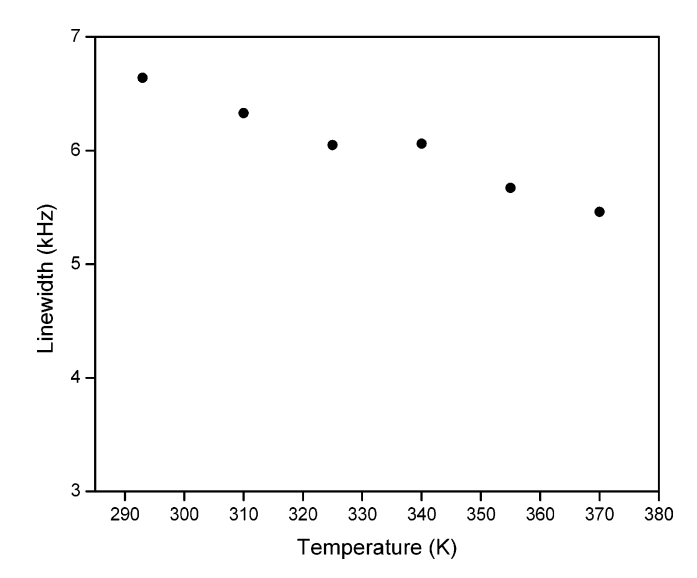

Figure 5. Line width versus temperature in LiBi$_4$Nb$_3$O$_{14}$.

700 °C, the measurements were made only up to 600 °C. Further the X-ray powder pattern of the sample indicates no change after the conductivity measurements. The reported results correspond to the heating cycle. Figure 6 shows the Arrhenius plot. The linear behavior of log σ with 1/*T* indicates the absence of any phase transition further confirmed by DTA up to 900 °C. The low values of conductivity even at high temperatures imply that conduction is mainly through oxide ions and not by lithium ions as supported by the structural evidence and ^{7}Li NMR studies. The interlinking of LiO$_4$ tetrahedra is such that it does not provide a continuous pathway for Li$^+$ migration hence both the compounds are poor lithium ion conductors.

To further confirm the poor mobility of lithium in the lattice of LiBi$_4$Nb$_3$O$_{14}$, Li$^+$/H$^+$ exchange studies were investigated in glacial acetic acid, concentrated hydrochloric acid, and nitric acid. The compound was stirred for 15 h in the acids and the products were washed thoroughly with distilled water and dried at 80 °C. The X-ray powder patterns before and after acid exchange showed no change, further supplemented by no differences in the IR spectra (see the Supporting Information, Figures S2 and S3). The absence of Li$^+$/H$^+$ exchange is consistent with the tetrahedral coordination of Li in this material.
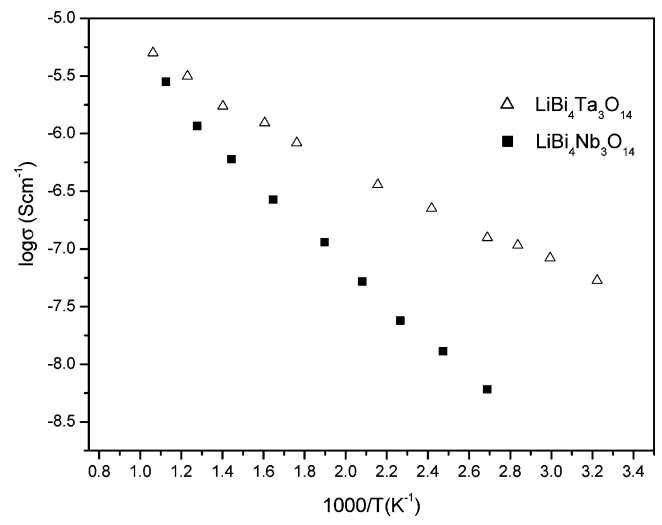
New Structural Variant of the Aurivillius Phase

J. Phys. Chem. B, Vol. 109, No. 23, 2005 **11447**

Figure 6. Conductivity Arrhenius plots of LiBi$_4$Ta$_3$O$_{14}$ and LiBi$_4$-Nb$_3$O$_{14}$.
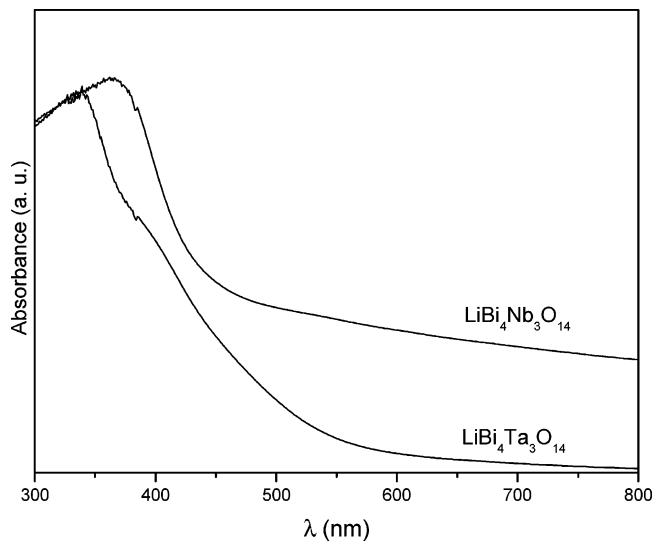
Figure 7. UV−visible diffuse reflectance spectra of LiBi$_4$Nb$_3$O$_{14}$ and LiBi$_4$Ta$_3$O$_{14}$.

Accordingly, this material does not exhibit Li$^+$/H$^+$ exchange even in concentrated acids.
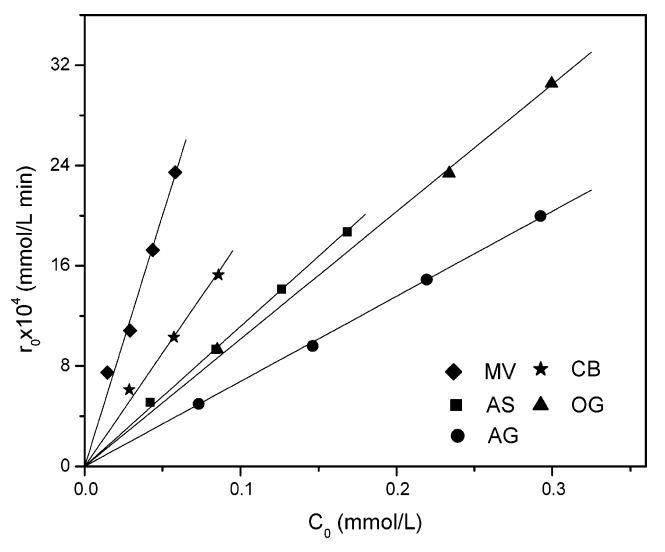
UV−Visible Spectra. The UV−visible diffuse reflectance spectra of LiBi$_4$Nb$_3$O$_{14}$ and LiBi$_4$Ta$_3$O$_{14}$ are shown in Figure 7. The measurements were made on polycrystalline samples of LiBi$_4$Ta$_3$O$_{14}$ and LiBi$_4$Nb$_3$O$_{14}$. To obtain precise values of band gap from the absorption edges the point of inflection determined from the minimum in the first derivative of the absorption spectrum were used. The values of band gap thus obtained for LiBi$_4$Ta$_3$O$_{14}$ and LiBi$_4$Nb$_3$O$_{14}$ correspond to 3.5 and 3.0 eV, respectively. Hence the band gap increases in the following manner: Ta^{5+} > Nb^{5+}.

Photocatalysis. Photocatalytic degradation of five commonly used dyes covering a wide range of visible spectrum (λ_{max} of dyes varying from 426 to 626 nm) and comprised of diverse functional groups such as sulfonate, amino, azo, hydroquinonic, and alkyl (methyl and ethyl) (see the Supporting Information, Table S1) was investigated. In addition, degradation of two phenolic compounds (phenol and 4-nitrophenol) was also investigated. No appreciable degradation of these compounds was observed either with UV or with LiBi$_4$Ta$_3$O$_{14}$ or LiBi$_4$-Nb$_3$O$_{14}$ alone. There was only about 2% reduction in the concentration of all compounds of interest when a solution of

100 ppm was stirred with LiBi$_4$Ta$_3$O$_{14}$ or LiBi$_4$Nb$_3$O$_{14}$ (at a loading of 2 kg/m^3) for 12 h in the dark. Therefore, the actual concentration of the solution was taken to be the initial concentration for kinetic analysis. All the photocatalytic degradation reactions were carried out at natural pH conditions. The initial concentration varied between 25 and 100 ppm for all dyes except for Methyl Violet, where a lower initial concentration of 5−20 ppm was investigated because of its high molar absorptivity (ϵ).

The degradation profiles of OG with an initial concentration of 100 ppm for different concentrations of LiBi$_4$Ta$_3$O$_{14}$ varying from 0.5 to 3 kg/m^3 are shown in the Supporting Information, Figure S4. The degradation profiles show a significant degradation of OG in the presence of both UV and LiBi$_4$Ta$_3$O$_{14}$ indicating the photocatalytic activity of LiBi$_4$Ta$_3$O$_{14}$ (E_g = 3.5 eV). The initial rates of the reaction were determined by extrapolating the tangent (based on the linear fit of the first 4−5 points) of the concentration profile (see the Supporting Information, Figure S4) back to initial conditions. The variation of initial rate with catalyst loading for the degradation of OG is shown in the Supporting Information, Figure S5. The initial rate of degradation increases with an increase in catalyst concentration from 0.5 to 2 kg/m^3 but saturates beyond a loading of 2 kg/m^3. This is consistent with the degradation of dyes in the presence of commercial catalysts such as TiO$_2$.[37,39,40] Therefore, a catalyst loading of 2 kg/m^3 was used to investigate the degradation of other compounds in this study.

The effect of initial concentration on the rate of photocatalytic degradation of OG was investigated over the concentration range of 25 to 100 ppm with 2 kg/m^3 of LiBi$_4$Ta$_3$O$_{14}$. The normalized degradation profiles of OG for different initial concentrations in the presence of LiBi$_4$Ta$_3$O$_{14}$ (see the Supporting Information, Figure S6a) show a continuous decrease in dye concentration in the first hour but later reach a limiting concentration. The normalized degradation profiles of AS, AG, CB, and MV for various initial concentrations in the presence of LiBi$_4$Ta$_3$O$_{14}$ are shown in the Supporting Information, Figures S6b−S6e. Degradation profiles of AS, AG, CB, and MV are similar to the degradation profile of OG with the initial degradation rate increasing with increasing initial concentration. However, the values of initial degradation rates and limiting concentrations depend on the nature of the dye and its initial concentration. To quantify the reactions, the following kinetic model is used. Heterogeneous photocatalytic reactions[37] normally follow Langmuir−Hinshelwood (LH) kinetics: $r_0 = k_0C_0/(1 + K_0C_0)$, where r_0 is the initial rate, C_0 is the initial concentration, k_0 is the kinetic rate constant, and the parameter K_0 represents the equivalent of the adsorption equilibrium coefficient. To determine the LH parameters, the above rate expression can be lineralized: $1/r_0 = (1/k_0)(1/C_0) + (K_0/k_0)$. This indicates that a plot of the reciprocal of initial rates ($1/r_0$) versus the reciprocal of initial concentration ($1/C_0$) would be linear. The parameters for photocatalytic degradation of OG, k_0 and K_0, obtained from the slope and intercept of the linear plot (shown in the inset of Figure S6a in the Supporting Information) are 0.011 min^{-1} and 0.00025 L/mmol, respectively. As K_0 represents the adsorption equilibrium coefficient, the low value of K_0 can be attributed to negligible adsorption. This is consistent considering that the BET surface area of LiBi$_4$Ta$_3$O$_{14}$ is 0.39 m^2/g, which is significantly lower than that of conventional catalysts ($\sim$50 m^2/g). This is further confirmed from X-ray powder patterns of the catalysts after the degradation reactions that indicate that the structure remains the same (see the Supporting Information, Figure S7) and no adsorption is observed. As the value of K_0 is

Figure 8. Variation of initial rates with concentration for photocatalytic degradation of MV, CB, AS, OG, and AG by $LiBi_4Ta_3O_{14}$.

TABLE 3: First Order Kinetic Rate Constants for the Degradation of Dyes and Phenolic Compounds

	catalyst	$k_0 \times 10^3 \, (min^{-1})$
compds dye		
AG	$LiBi_4Ta_3O_{14}$	6.8
AS	$LiBi_4Ta_3O_{14}$	12
OG	$LiBi_4Ta_3O_{14}$	11.4
CB	$LiBi_4Ta_3O_{14}$	24.2
MV	$LiBi_4Ta_3O_{14}$	58.8
AG	$LiBi_4Nb_3O_{14}$	3.8
AS	$LiBi_4Nb_3O_{14}$	5.7
organic compds		
phenol	$LiBi_4Ta_3O_{14}$	2.4
	$LiBi_4Nb_3O_{14}$	3.9
4-nitrophenol	$LiBi_4Ta_3O_{14}$	2.2
	$LiBi_4Nb_3O_{14}$	3.2

very small, $K_0C_0 \ll 1$ and the LH rate expression reduces to a first-order rate expression: $r_0 = k_0C_0$. The linear dependency of initial rates, r_0, and initial concentrations, C_0, for all dyes in Figure 8 confirms the first-order kinetics of photocatalytic degradation of dyes with $LiBi_4Ta_3O_{14}$. The overall kinetic rate constants of degradation of dyes determined from the slope of the linearly regressed lines (Figure 8) of initial rates and initial concentrations are shown in Table 3. The order of degradation is MV > CB > AS > OG > AG. The initial rate of degradation of OG with $LiBi_4Ta_3O_{14}$ is comparable to the initial rate of degradation with commercial Degussa P-25 catalyst.[37] Since $r_0 = -dC_0/dt = k_0C_0$, this can be solved to obtain $\ln(C/C_0)$, which indicates a semilog plot of the ratio of concentration at any time t to the initial concentration with reaction time would be linear.

The photocatalytic degradation profiles of AS and AG with $LiBi_4Nb_3O_{14}$ as catalyst are shown in the Supporting Information, Figure S8. The linear plot (inset of Figure S8) of $\ln(C/C_0)$ with time confirms that the initial rate of degradation is first order. The other dyes CB, OG, and MV did not degrade in the presence of $LiBi_4Nb_3O_{14}$. This is probably due to the preferential affinity of niobium toward the phenolic and quninonic groups present in both AG and AS and absent in the other dyes. Hence, substitution of Nb for Ta in $LiBi_4M_3O_{14}$ alters the photocatalytic behavior of the compound. Inspite of the lower band gap in $LiBi_4Nb_3O_{14}$ ($E_g = 3$ eV) compared to $LiBi_4Ta_3O_{14}$ ($E_g = 3.5$ eV), the degradation rates of both AS and AG were lower in $LiBi_4Nb_3O_{14}$ than in $LiBi_4Ta_3O_{14}$. This could probably be due to the selectivity of $LiBi_4Nb_3O_{14}$ for phenolic and quinonic groups only while $LiBi_4Ta_3O_{14}$ could attack all functional groups

of the dyes and phenolic compounds, which is evident from the catalytic activity of $LiBi_4Ta_3O_{14}$ over $LiBi_4Nb_3O_{14}$ for CB, OG, and MV.

To substantiate the hypothesis that $LiBi_4Nb_3O_{14}$ selectively degrades phenolic compounds, the photoreactivity of two phenols (phenol and 4-nitrophenol) in the presence of $LiBi_4$-Nb_3O_{14} and $LiBi_4Ta_3O_{14}$ was investigated. The degradation profiles of the phenols (see the Supporting Information, Figure S9) indicate that the initial rates of degradation of phenolic compounds also follow first-order kinetics and the kinetic rate constants determined from the slope of that linear plot are given in the inset of Figure S9 in the Supporting Information. 4-Nitrophenol degraded faster than phenol for both catalysts, which is consistent with the degradation of these compounds with commercial catalyst.[41]

In case of phenolic compounds, $LiBi_4Nb_3O_{14}$ shows higher photocatalytic activity over $LiBi_4Ta_3O_{14}$, which is consistent with its characteristics of lower band gap and selectivity for phenolic functional groups. Thus both $LiBi_4Ta_3O_{14}$ and $LiBi_4$-Nb_3O_{14} exhibit reasonable photocatalytic activity in degrading some of the dyes and organic compounds despite their low surface area of 0.3 and <0.1 m²/g, respectively, compared to a commercial catalyst like Degussa P-25.

Summary

$LiBi_4Nb_3O_{14}$ and $LiBi_4Ta_3O_{14}$ were synthesized and characterized by single-crystal X-ray diffraction to depict a structure that has similarities with an ideal Aurivillius phase and a typical hexagonal tungsten bronze. Subtle changes in coordination around the Bi atoms are evidenced though the packing motifs of $LiBi_4Nb_3O_{14}$ and $LiBi_4Ta_3O_{14}$ are the same. The arrangement of the Li atoms with respect to the Nb/Ta atoms is a unique feature in the crystal structures of these compounds and the fact that there is no interlinking between the LiO_4 tetrahedra rules out the possibility of ionic conductivity due to Li ions further supplemented by the variable-temperature ⁷Li NMR and Li⁺/ H⁺ exchange studies. The ionic conductivity of the order of 10^{-6} S cm^{-1} indicates that both the compounds are semiconductors. $LiBi_4Nb_3O_{14}$ and $LiBi_4Ta_3O_{14}$ show low band gaps of 3.0 and 3.5 eV, respectively. These compounds have been demonstrated to degrade specific dyes and phenolic compounds effectively. $LiBi_4Nb_3O_{14}$, however, shows selectivity in the degradation of dyes.

Supporting Information Available: CIFs of $LiBi_4Nb_3O_{14}$ and $LiBi_4Ta_3O_{14}$; ⁷Li NMR spectrum of a static sample of $LiBi_4$-Ta_3O_{14} (Figure S1); powder X-ray patterns of (a) simulated (b) synthesized samples of $LiBi_4Nb_3O_{14}$ after addition of (a) HCl, (b) HNO₃, and (e) glacial acetic acid (Figure S2); IR spectra of $LiBi_4Nb_3O_{14}$ (a) before addition of acid and after addition of (b) HCl, (c) HNO₃, and (d) glacial acetic acid (Figure S3); photocatalytic degradation profile of OG $LiBi_4Ta_3O_{14}$ at various catalyst loading (Figure S4); variation of initial rate with catalyst loading for the degradation of OG by $LiBi_4Ta_3O_{14}$ (Figure S5); photocatalytic degradation profles of (a) OG, (b) AS, (c) AG, (d) CB, and (e) MV in the presence of 2 kg/m³ of $LiBi_4Ta_3O_{14}$ (Figure S6); X-ray powder patterns of $LiBi_4Nb_3O_{14}$ and $LiBi_4$-

Ta_3O_{14} after the degradation of Alizarin Red dye (Figure S7); photocatalytic degradation profiles of AS and AG in the presence of 2 kg/m^3 of $LiBi_4Nb_3O_{14}$ (Figure S8); photocatalytic degradation profiles of phenol and 4-nitrophenol in the presence of 2 kg/m^3 of $LiBi_4Nb_3O_{14}$ and $LiBi_4Ta_3O_{14}$ (Figure S9); structure of dyes (Table S1). This material is available free of charge via the Internet at http://pubs.acs.org. The crystal data has been deposited at the Fachinformationszentrum Karlsruhe (FIZ) with the numbers CSD 391261 and CSD 415141.

References and Notes

(1) Moro-Oka, Y.; Ueda, W. *Adv. Catal.* **1994**, *40*, 233.

(2) Park, B. H.; Kang, B. S.; Bu, D. S.; Noh, T, W.; Lee, J.; Jo, W. *Nature* **1999**, *401*, 682.

(3) Boivin, J. C.; Mairesse, G. *Chem Mater.* **1998**, *10*, 2870.

(4) Keve, E. T.; Skapski, A. C. *J. Chem. Soc. A* **1971**, 1280.

(5) Keve, E. T.; Skapski, A. C. *J. Solid State Chem.* **1973**, *8*, 159.

(6) Subramanian, M. A.; Calabrese, J. C. *Mater. Res. Bull.* **1993**, *28*, 523.

(7) Castro, A.; Aguado, E.; Rojo, J. M.; Herrero, P.; Enjalbert, R.; Galy, J. *Mater. Res. Bull.* **1998**, *33*, 31.

(8) Ling, C. D.; Schmis, S.; Withers, R. L.; Thompson, J. G.; Ishizawa, N.; Kishimoto, S. *Acta Crystallogr. B* **1999**, *55*, 157.

(9) Ling, C. D.; Thompson, J. G.; Withers, R. L.; Schmid, S. *J. Solid State Chem.* **1999**, *142*, 33.

(10) Lee, C.-Y.; Marquart, R.; Qing-Di, Z.; Kennedy, B. J. *J. Solid State Chem.* **2003**, *174*, 310.

(11) Zou, Z.; Ye, J.; Arakawa, H. *Chem. Phys. Lett.* **2001**, *333*, 57.

(12) Sayama, K.; Yase, K.; Arakawa, H.; Asakura, K.; Tanaka, K.; Domen, K.; Onishi, T. *J. Photochem. Photobiol.*, *A* **1998**, *114*, 125.

(13) Takata, T.; Tanaka, A.; Hara, M.; Kondo, J.; Domen, K. *Catal. Today* **1998**, *44*, 17.

(14) Zou, Z.; Ye, J. *J. Alloys Compd.* **1999**, *292*, 72.

(15) Hoffmann, M. R.; Martin, S. T.; Choi, W.; Bahnemann, D. W. *Chem. Rev.* **1995**, *95*, 69.

(16) Mills, G.; Hoffmann, M. R. *Environ. Sci. Technol.* **1993**, *27*, 1681.

(17) Kormann, C.; Bahnemann, D. W.; Hoffmann, M. R. *Environ. Sci. Technol.* **1991**, *25*, 494.

(18) Carraway, E. R.; Hoffman, A. J.; Hoffmann, M. R. *Enuiron. Sci. Technol.* **1994**, *28*, 786.

(19) Chemeseddine, A.; Boehm, H. P. *J. Mol. Catal.* **1990**, *60*, 295.

(20) D'Oliveira, J. C.; Minero, C.; Pelizzetti, E.; Pichat, P. *J. Photochem. Photobiol.*, *A* **1993**, *72*, 261.

(21) D'Oliveira, J. C.; Al-Sayyed, G.; Pichat, P. *Environ. Sci. Technol.* **1990**, *24*, 990.

(22) Hidaka, H.; Zhao, J.; Pelizzetti, E.; Serpone, N. *J. Phys. Chem.* **1992**, *96*, 2226.

(23) Pelizzetti, E.; Minero, C.; Piccinini, P.; Vincenti, M. *Coord. Chem. Rev.* **1993**, *125*, 183.

(24) Albert, M.; Gao; Y. M.; Toft, D.; Dwight, K.; Wold, A. *Mater. Res. Bull.* **1992**, *71*, 961.

(25) Inel, Y.; Ertek, D. *J. Chem. Soc.*, *Faraday Trans.* **1993**, *89*, 129.

(26) Borgarello, E.; Serpone, N.; Emo, G.; Harris, R.; Pelizzetti, E.; Minero, C. *Inorg. Chem.* **1986**, *25*, 4449.

(27) Ollis, D. F.; Pelizzetti, E.; Semone, N. *Environ. Sci. Technol.* **1991**, *25*, 1523.

(28) Zou, Z.; Ye, J.; Arakawa, H. *Chem. Phys. Lett.* **2001**, *333*, 57.

(29) Beskrovnyi, A. I.; Vasilevskii, S. G.; Belushkin, A. V.; Smirnov, L. S.; Balagurov, A. M.; Martinez Sarrion, M. L.; Mestres, L.; Herriaz, M. *Kristallografiya* **2003**, *48*, 440.

(30) Aurivillius, B. *Ark. Kemi.* **1950**, *2*, 19.

(31) Choy, J.-H.; Kim J−Y.; Chung, I. *J. Phys. Chem. B* **2001**, *105*, 7908.

(32) SMART (Version 5.625), SAINT (Version 6.45a), RLATT (Version 3.0); Bruker AXS Inc.: Madison, WI, 2000.

(33) Sheldrick, G. M. SHELXL97, Program for crystal structure refinement; University of Gottingen: Gottingen, Germany, 1997.

(34) Brown, I. D.; Shannon, R. D. *Acta Crystallogr. A* **1973**, *29*, 266.

(35) Brown, I. D.; Altermatt, D. *Acta Crystallogr. B* **1985**, *41*, 244.

(36) Grenier, J. C.; Bassi, G *Bull. Soc. Fr. Mineral. Cristallogr.* **1965**, *88*, 345.

(37) Sivalingam, G.; Nagaveni, K.; Hegde, M. S.; Madras, G. *Appl. Catal.*, *B* **2003**, *45*, 23.

(38) Kudo, T.; Oi, J.; Kishimoto, A.; Hira *Mater. Res. Bull.* **1991**, *26*, 779.

(39) Habibi, M, H.; Hassanzadeh, A.; Mahdavi, H. *J. Photochem. Photobiol.*, *A* **2005**, *172*, 89.

(40) Daneshvar, N.; Rabbani, M.; Modirshahla, N.; Behnajady, M. A. *J. Photochem. Photobiol.*, *A* **2004**, *168*, 39.

(41) Nagaveni, K.; Sivalingam, G.; Hegde, M. S.; Madras, G. *Environ. Sci. Technol.* **2004**, *38*, 1600.